ADVANCED ENERGY MATERIALS
www.advenergymat.de

Superionic Fluorinated Halide Solid Electrolytes for Highly Stable Li-Metal in All-Solid-State Li Batteries

Tianwei Yu, Jianwen Liang, Liang Luo, Limin Wang, Feipeng Zhao, Guofeng Xu, Xiangtao Bai, Rong Yang, Shangqian Zhao, Jiantao Wang, Jinqiu Yu,* and Xueliang Sun**

The halide solid-state electrolytes (SSEs) have received significant attention due to their high ionic conductivity and desirable compatibility with cathode materials. However, the reduction potential of the halide is still >0.6 V (versus Li/Li$^+$). Reduction stability is still one of the challenges that need to be addressed. The fluorides have a wide electrochemical stability window due to the large electronegativity of F$^-$. In contrast, Li_3YBr_6 (LYB) bromides have a narrower electrochemical window, although they have high lithium ion conductivity (>10^{-3} S cm^{-1}). Herein, a fluorine doping strategy is employed. The interfacial stability between fluoride-doped bromides and lithium metal is researched by cycling of lithium symmetric cells. Li plating/stripping can maintain over 1000 h at 0.75 mA cm^{-2}. Interfacial protection mechanisms investigated by X-ray photoelectron spectroscopy. A fluoride-rich interfacial layer is formed in situ during the cycle, which achieves inhibition of the reduction. The Li metal treated fluorine doping of LYB exhibits significant potential in full cells. In fact, the induction of a stable in situ interfacial layer by fluorine doping can effectively improve the interfacial stability of bromides to lithium metal. Fluorine-doped modification offers a new attempt to realize lithium metal applications in all-solid-state lithium batteries.

1. Introduction

All-solid-state lithium batteries (ASSLBs) become the focus of extensive research in order to achieve high energy density in energy storage technology with excellent safety conditions.[1] As the main components of ASSLBs, the solid-state electrolytes (SSEs) play an essential role in ASSLBs.[2] Over the past few years, researches on inorganic solid electrolytes have made significant progress.[3,4]

After decades of research effort, various lithium solid electrolytes with high ionic conductivity were developed, including oxide, sulfide, polymer, halide, etc. Among these materials, oxide solid electrolytes such as perovskite-type $Li_{3/8}Sr_{7/16}Ta_{3/4}Zr_{1/4}O_3$,[5] sodium super ionic conductor type $Li_{1.5}Al_{0.5}Ti_{1.5}(PO_4)_3$,[6] and garnet-type $Li_{6.4}La_3Zr_{1.4}Ta_{0.6}O_{12}$[7] could reach the level of ≈10^{-4}–10^{-3} S cm^{-1} at room temperature. However, the poor physical contact due to the inherent mechanical rigidity of oxide SSEs cause hindered ion transport at the interface.[8] At the same time, a high reaction temperature is required in the preparation process, which makes the manufacturing cost high.[9] These problems can be avoided for the ductile sulfide SSEs due to intimate good ionic contacts. For example, thio-lithium super ionic conductor type $Li_{3.25}Ge_{0.25}P_{0.75}S_4$,[10] glass type Li_2S-B_2S_3-SiO_2-LiI,[11] glass-ceramic type $Li_7P_3S_{11}$,[12] Argyrodite type Li_6PS_5Cl,[13] $Li_{10}GeP_2S_{12}$,[14] and $Li_{9.54}Si_{1.74}P_{1.44}S_{11.7}Cl_{0.3}$[15] exhibit superionic

T. Yu, G. Xu, X. Bai, R. Yang, S. Zhao, J. Wang
National Power Battery Innovation Center
GRINM Group Co. Ltd.
Beijing 100088, P. R. China
E-mail: jiantaowang2002@126.com

T. Yu, G. Xu, X. Bai, R. Yang, S. Zhao, J. Wang
China Automotive Battery Research Institute Co., Ltd.
Beijing 100088, P. R. China

T. Yu, G. Xu, X. Bai, R. Yang, S. Zhao, J. Wang
General Research Institute for Nonferrous Metals
Beijing 100088, P. R. China

J. Liang, F. Zhao, X. Sun
Department of Mechanical and Materials Engineering
University of Western Ontario
London, Ontario N6A 5B9, Canada
E-mail: xsun9@uwo.ca

L. Luo, J. Yu
National Engineering Research Center for Rare Earth Materials
GRINM Group Co., Ltd.
Beijing 100088, P. R. China
E-mail: yujinqiu@mail.ipc.ac.cn

L. Luo, J. Yu
Rare Earth Functional Materials (Xiong'an) Innovation Center Co., Ltd.
Xiong'an 071700, P. R. China

L. Wang
General Research Institute for Nonferrous Metals
Beijing 100088, P. R. China

L. Wang
GRIMAT Engineering Institute Co. Ltd.
Beijing 100088, P. R. China

The ORCID identification number(s) for the author(s) of this article can be found under https://doi.org/10.1002/aenm.202101915.

DOI: 10.1002/aenm.202101915

conductivities (≈10^{-3}–10^{-2} S cm^{-1}) without sintering process. The instability of sulfide SSEs under high potential limit its application with 4 V cathode materials.[16] Buffer coating layer must be introduced, such as $Li_4Ti_5O_{12}$[4] and $LiNbO_3$.[17] The main disadvantage is that the lower ionic conductivity of the buffer layer ($LiNbO_3$: 10^{-5} S cm^{-1}) may hinder ion transmission.[18]

In order to find SSEs that are oxidation stable at high potentials, halides have recently been reconsidered as suitable candidates. The newly developed halide SSEs such as Li_3InCl_6 (LIC),[19] Li_3YCl_6 (LYC)/Li_3YBr_6,[20] $Li_3Er(Y)Cl_6$,[21] Li_3ScCl_6,[22] $Li_2Sc_{2/3}Cl_4$,[23] and $Li_{2.5}Er_{0.5}Zr_{0.5}Cl_6$[24] show high level of conductivities (≈10^{-4}–10^{-3} S cm^{-1}). Besides, halide electrolytes have obvious advantages in electrochemical windows, especially fluoride and chloride. Mo et al. reported the calculation and analysis of electrochemical windows for various electrolytes and oxidation potential of chloride electrolytes exceeds 4.2 V (versus Li^+/Li).[25] Besides, Fajan et al. believe that halide electrolytes have more covalent bonds than sulfide electrolytes. The lattice structure of halide electrolytes is softer, which mean halide electrolytes have better machining performance.[26] Therefore, halide SSEs are regarded as a potential SSEs for ASSLBs.[27] Han et al. evaluated crossover experiments on full cells with single-crystal or poly-crystal $LiNi_{0.88}Co_{0.11}Al_{0.01}O_2$ (NCA) loaded with LYC or $Li_6PS_5Cl_{0.5}Br_{0.5}$ electrolytes.[28] By engineering the electrode preparation, single-crystal NCA particles can achieve favorable wettability with LYC particles, whose full cells have an excellent electrochemical stability and achieve an impressive performance of nearly 97% capacity retention after 200 cycles. The LYC-equipped full cell has potential for commercial application.

The most promising applications of solid-state batteries are reliant upon the use of Li metal anodes, which are desirable due to their high specific capacity of 3860 mAh g^{-1} and low electrochemical potential. Although halide electrolytes reveal high ionic conductivity and oxidation stable at high potentials, there are not any reports about the capacity of usage in Li anode. The poor stability at the interface of the Li metal and halide SSEs is still a challenge. The electrochemical window of Li_3InCl_6 halide SSEs is 2.5–4.3 V (versus Li^+/Li).[25] Although reduction stability of the group IIIB elements is much better than that of the group IIIA metal ions, the electrochemical window of Li_3YCl_6/Li_3YBr_6 halide SSEs is 0.62–4.21 V/ 0.59–3.15 V (versus Li^+/Li).[20] Halide solid electrolytes with group IIIB elements still cannot achieve stable matching to lithium metal. Riegger et al. concluded that a reduction reaction between the halide solid-state electrolyte LIC and LYC and lithium metal is inevitable.[29] LiCl and oxides, decomposition products of LIC and LYC, were found by in situ X-ray photoelectron spectroscopy. This electrochemical instability precludes the use of halide solid-state electrolytes in solid-state batteries with lithium metal anode. Continuous generation of high resistance interface products can severely impede lithium-ion diffusion. At the same time, degradation of the solid electrolyte leads to the destruction of the interfacial structure. Cracks or voids occur at the interface on one side of the solid electrolyte where lithium dendrites tend to grow. The growth of lithium dendrites would lead to internal short circuits, eventually.[30] Riegger et al. suggested that Li_6PS_5Cl can achieve stable solid–electrolyte interphase (SEI) formation.[29] However, the introduction of a new electrolyte layer would complicate the cell preparation process and is not conducive to large-scale applications.

According to theoretical predictions, the reduction potential of the halide solid-state electrolyte is still >0.6 V (versus Li/Li^+), showing that these electrolytes can be used in contact with most high voltage anode such as In, $Li_4Ti_5O_{12}$, etc., but the anode interface may be unstable in Li anode. Due to the expected instability against the Li metal anode, sulfide solid state electrolyte such as Li_6PS_5Cl as a separator layer is mostly used, and the halide SSEs are primarily used in cathode parts. Unfortunately, no theoretical and experimental studies on the design for the interface stability of halide SSEs against the Li metal anode have been reported.

Here, we report a new metal-halide electrolyte, fluorinated $Li_3YBr_{5.7}F_{0.3}$, not only with high ionic conductivity (1.8×10^{-3} S cm^{-1}) but also can directly work with Li metal anode. Due to the high stability of interface from the in situ formation of F-rich component in Li plating and stripping process, Li symmetric cells with $Li_3YBr_{5.7}F_{0.3}$ as electrolyte can exhibit high stability over 1000 h at 0.75 mA cm^{-2} with the capacity of 0.75 mAh cm^{-2}. Detailed analysis suggests that the in situ surface between the Li metal and designed $Li_3YBr_{5.7}F_{0.3}$ electrolyte exhibits a high concentration of fluoride. The in situ fluorinated layers form better contact area. The in situ fluoride layer is homogeneously distributed at the interface, which contributes to high cycle stability. Moreover, all-solid-state batteries by directly using Li metal as anode and $LiCoO_2$ (LCO) as cathode demonstrate high cycling stability at room temperature. Our results identify promising oxidation stable halide-based lithium superionic conductors which also can be used against Li anode.

2. Results and Discussion

By the high-temperature solid-state reaction, YBr_3 was substituted with different amounts of YF_3 to synthesize a series of $Li_3YBr_{6-x}F_x$. The SSEs were protected by Kapton film from air to conduct the measurements of X-ray diffraction (XRD). The phase composition of $Li_3YBr_{5.7}F_{0.3}$ is displayed in **Figure 1**a. The XRD patterns of $Li_3YBr_{5.7}F_{0.3}$ are similar with that of Li_3YBr_6 in literature report.[20] Close-packed-like anion sublattice forms the basic structure of $Li_3YBr_{5.7}F_{0.3}$, belonging to the cubic close-packed (ccp) arrangement. Li_3YBr_6 is isomorphs of Li_3ErBr_6 (ICSD No. 50182, space group C2/m). The Rietveld refinement and crystal structural information is shown in FigureS2 and Table S1, Supporting Information. With the increasing of fluorination, no obvious changes in peak distribution. The main characteristic peak around 31.7° of Li_3YBr_6 shifts to a larger angle when compare with the diffraction peak of $Li_3YBr_{5.7}F_{0.3}$. According to the Bragg's Law, F doping leads to a smaller lattice size, which increases the peak angle (≈0.1°) (Figure 1b). The other ratio of the materials are based on the chemical composition of $Li_3YBr_{6-x}F_x$ (x = 1,2,3), as shown in Figure S1a, Supporting Information, when x increases to 1, the diffraction peaks of LiBr and YF_3 can be distinguished. As the fluorine doping continues to increase, the peak intensities of LiBr and YF_3 gradually increase. When x = 3, the peaks of Li_3YBr_6 almost completely disappeared, which indicates that the fluorine doping is saturated when $x \geq 1$. Excessive doping

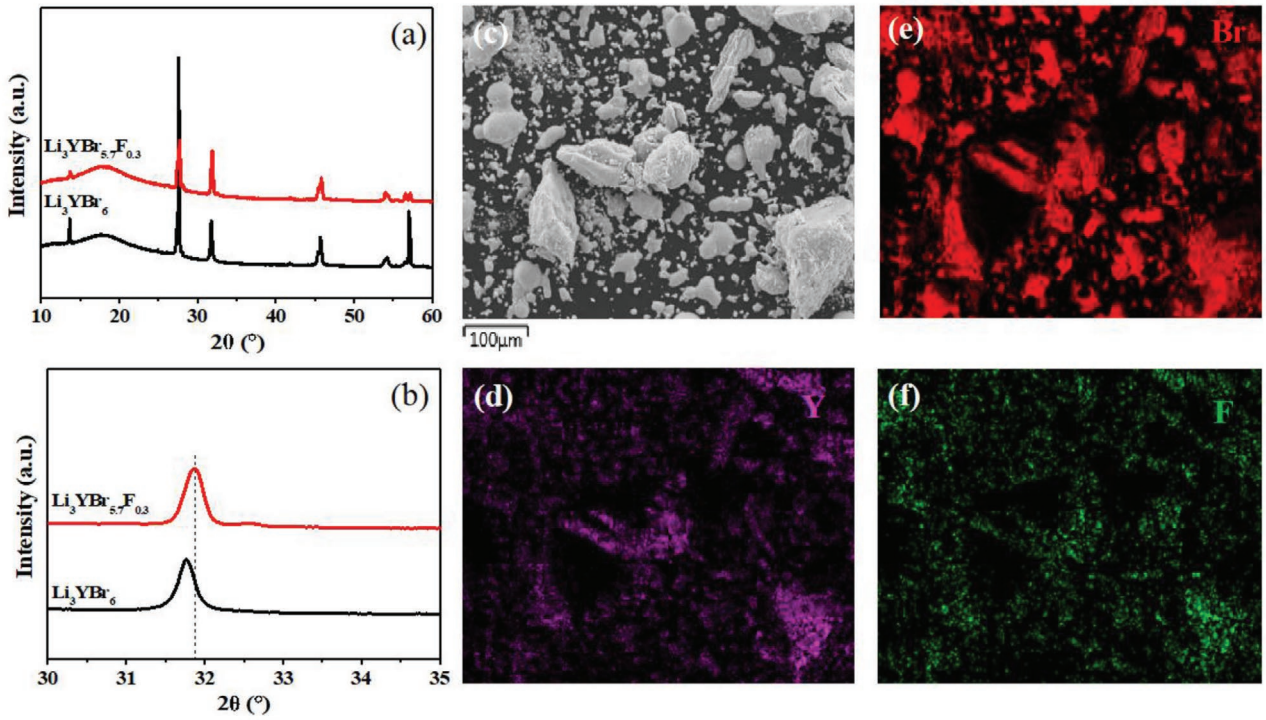

Figure 1. Characterizations of electrolytes. a,b) XRD patterns of the $Li_3YBr_{5.7}F_{0.3}$ and Li_3YBr_6. c) SEM image of the $Li_3YBr_{5.7}F_{0.3}$. d–f) EDS element mapping of the image of (c).

leads to the appearance of the impurity phase. Also, the peak angle shift when $x = 1$ is similar to $x = 0.3$(Figure S1b, Supporting Information). It is suggested that fluorine doping is close to saturation for $Li_3YBr_{5.7}F_{0.3}$. In order to further confirm the saturation of the F-doping, density functional theory (DFT) calculation were taken. The enthalpy changes (ΔH(F)) of the $Li_3YBr_{6-x}F_x$ was calculated by the following Equation (1):

$$\Delta H(F) = E(Li_{24}Y_8Br_{48-x}F_x) - 24E(LiBr) - (8 - x/3)E(YBr_3) - x/3E(YF_3) \quad (1)$$

The E means the binding energy of the compound. The ΔH(F) is 0.33 eV/atom when doping one F atom in a supercell ($2 \times 1 \times 2$), while the average ΔH(F) of each F atom is 0.29 eV/atom when doping multiple F atoms, which indicates that F doping is a non-spontaneous process and requires external energy. When the reaction temperature range is chosen to be 900–1000 °C, the F doping concentration limit is calculated by the following Equation (2):

$$C_F = C_0 * EXP(-\Delta H(F)/k_BT),\ C_{Br} = C_0 * EXP(-\Delta H(Br)/k_BT)$$
$$C_F/C_{Br} = x/6,\ x = 6EXP(-\Delta H(F)/k_BT) \quad (2)$$

The C means the concentration of the element, while the C0 means the initial concentration and the T means the temperature. The upper limit of F-doping concentration is calculated to be $x = 0.37$ and the lower limit is $x = 0.25$ at 950 °C. Thus, the average value of the F-doping limit is 0.31, which corresponds to the XRD results (**Table 1**). The morphology of the Li_3YBr_6 and $Li_3YBr_{5.7}F_{0.3}$ was analyzed by scanning electron microscopy (SEM). Both SSEs showed spherical particles with micron-size (Figure S3, Supporting Information). Li_3YBr_6 spherical secondary particles are composed of primary lamellar particles the primary particles of $Li_3YBr_{5.7}F_{0.3}$ are much thicker, and the interlamellar layers are significantly filled, which indicates an increase in $Li_3YBr_{5.7}F_{0.3}$ densities after doping. The selected area were studied by energy disperse spectroscopy element mapping. As shown in Figure 1c–f, the elements Y, Br, and F are homogeneously distributed in $Li_3YBr_{5.7}F_{0.3}$. The elements Y and Br are homogeneously distributed as well in Li_3YBr_6 (Figure S4, Supporting Information).

The ionic conductivity of $Li_3YBr_{5.7}F_{0.3}$ was analyzed by electrochemical impedance spectroscopy (EIS). As shown in **Figure 2**b, the ionic conductivity of Li_3YBr_6 can reach 2.1×10^{-3} S cm^{-1}. The activation energy is calculated at 0.378 eV (Figure 2b), which is similar to Asano's report.[20] The ionic conductivity of $Li_3YBr_{5.7}$ $F_{0.3}$ can still maintain at 1.8×10^{-3} S cm^{-1}. There is no significant increase in the activation energy, which keeps at 0.39 eV (Figure 2b). In addition to $Li_3YBr_{5.7}F_{0.3}$, larger fluorine doping electrolytes were also synthesized. Excessive fluorine doping also affects ionic conductivity. When $x = 1$, the

Table 1. F-doping concentration limits at different reaction temperature.

T [°C]	C [F]≈Lower limit	C [F]≈Upper limit
900	0.22	0.33
950	0.25	0.37
1000	0.28	0.41

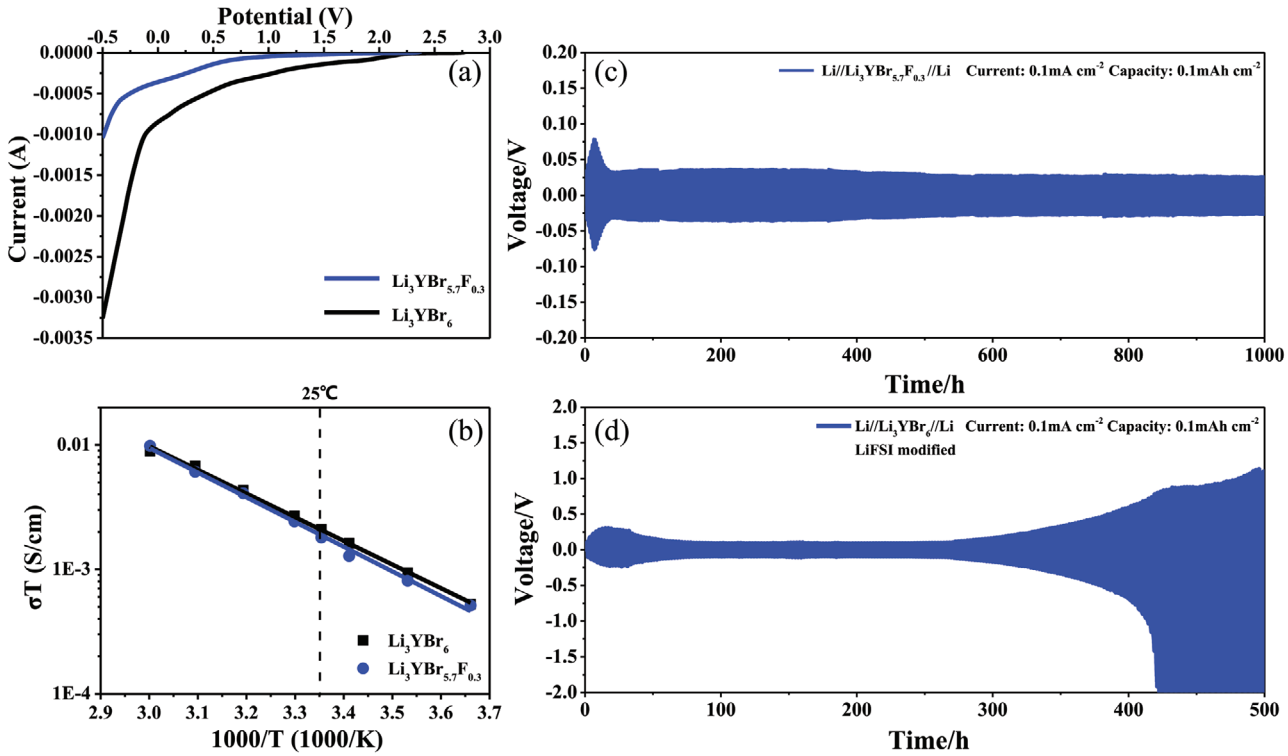

Figure 2. Electrochemical characteristics of electrolytes. a) LSV curve of the Li_3YBr_6 and $Li_3YBr_{5.7}F_{0.3}$. b) Arrhenius plots of the $Li_3YBr_{5.7}$ $F_{0.3}$ and Li_3YBr_6. c,d) Li symmetric cells. Li plating and stripping in c) $Li//Li_3YBr_{5.7}F_{0.3}//Li$ symmetric cells at 0.1 mA cm^{-2} with the capacity of 0.1 mAh cm^{-2} and d) $Li//Li_3YBr_6//Li$ symmetric cells at 0.1 mA cm^{-2} with the capacity of 0.1 mAh cm^{-2} with LiFSI modified.

ionic conductivity deceases to 8.8 × 10^{-4} S cm^{-1}. And when x = 2, the ionic conductivity is only 4.6 × 10^{-4} S cm^{-1} due to the excess fluoride remaining (Figure S5a, Supporting Information). Continuously decreasing levels of ionic conductivity are closely linked to an increase in the proportion of impurities. The results of EIS agree well with the results of XRD. The electronic conductivity of $Li_3YBr_{5.7}F_{0.3}$ was calculated by steady current value of direct current polarization curves based on Ohm's law. As shown in Figure S5b, Supporting Information, the electronic conductivity of $Li_3YBr_{5.7}F_{0.3}$ is 4.77 × 10^{-9} S cm^{-1}, which is 10^6 times lower than the ionic conductivity of $Li_3YBr_{5.7}F_{0.3}$. Such a difference between the ionic and electronic conductivity demonstrates the electronic insulating properties and the high lithium ion conductivity of the $Li_3YBr_{5.7}F_{0.3}$.

As exhibited in Figure 2a, the linear sweep voltammetry (LSV) curve of CNT/Li_3YBr_6 //Li_3YBr_6 //Li cell climbs up at 2.0 V, and the current density dramatically increases around 0.5 V. In contrast, CNT/$Li_3YBr_{5.7}F_{0.3}$//$Li_3YBr_{5.7}F_{0.3}$//Li cell maintains a low current density. The absolute value of the reduction currents for $Li_3YBr_{5.7}F_{0.3}$ is 0.001A at −0.5 V, which is lower than Li_3YBr_6 of 0.00325A at −0.5 V. Both the absolute values of the reduction currents of the cells with $Li_3YBr_{5.7}F_{0.3}$ or Li_3YBr_6 are in the high magnitude range, indicating that the $Li_3YBr_{5.7}F_{0.3}$ or Li_3YBr_6 are still unstable to lithium metal. The curves are further integrated (from 2.0 to −0.6 V) to quantify electrochemical stability. The integrated current of $Li_3YBr_{5.7}F_{0.3}$ is 5.8 × 10^{-4} AV cm^{-1}, which is smaller than Li_3YBr_6 of 2.7 × 10^{-3} AV cm^{-1}. It is demonstrated that the $Li_3YBr_{5.7}F_{0.3}$ have slower polarization than Li_3YBr_6. F doping suppresses the processes of reduction reaction effectively.

The interface stability between Li metal and $Li_3YBr_{5.7}F_{0.3}$ was studied by cycling Li–Li symmetrical cells. As demonstrated in Figure 2c, under current density of 0.1 mA cm^{-2}, the initial plating/stripping potential of the cell with $Li_3YBr_{5.7}F_{0.3}$ is around 0.05 V. With the initial activation process, the plating/stripping potential increases to a maximum of 0.09 V due to the interface reaction. Such a large potential change proves that the original interface is unstable. The results of cycling Li–Li symmetrical cells agree well with the results of linear sweep voltammetry (LSV). The plating/stripping potential gradually drops around 0.05 V as the cycle continues. It is well known that a solid–solid contact is achieved between the solid-state electrolyte layer and the lithium metal electrode. The surface of the solid phase is extremely rough. Therefore, the physical contact at the interface of the solid phase is also extremely poor. There are many micro voids or gaps at the interface between the solid-state electrolyte layer and the lithium metal electrode. As mentioned above, the bromides are chemically unstable with the lithium metal before and after doping and there are violent interfacial reactions that occur during cycling. The products of the interfacial reaction tend to fill the micro voids or gaps at the interface and gradually form an in situ interfacial layer between the solid-state electrolyte layer and the lithium metal electrode, which greatly enhances the contact performance of the solid-state electrolyte layer and the lithium metal electrode. As a result, polarization and resistance decreased upon cycling for the symmetric cells due to the formation of the higher area contact. The plating/stripping potential could maintain at a steady cycle of 0.05 V. It is mean that the in situ formed interphase between Li and $Li_3YBr_{5.7}F_{0.3}$ is robust, which can limit

the degradation of electrolyte during cycling. Even reach 1000 h, the cell remains stable without the increase of polarization. The plating/stripping potential of the cell with pure Li_3YBr_6 exhibits a similar trend to the cell with $Li_3YBr_{5.7}F_{0.3}$ at the first 50 h (Figure S6a, Supporting Information). By contrast, the plating/stripping potential is gradually increasing after 50 h, which indicated that the interface reaction is constantly on-going without inhibition. The plating/stripping potential even reaches 1.0 V around 500 h, which means that the interfacial reaction is not inhibited. The accumulation of interfacial side products increases the interfacial transfer resistance, further increasing the polarization phenomenon. After 500 h, short circuits occur eventually due to the growth of lithium dendrite.

The cell with $Li_3YBr_{5.7}F_{0.3}$ can effectively limit interface reaction and guarantee long cycling durability due to the robust $Li/Li_3YBr_{5.7}F_{0.3}$ interface. In order to assess the limits of the lithium plating/stripping capacity of the $Li_3YBr_{5.7}F_{0.3}$, the critical current density (CCD) was measured for lithium symmetric cells under different multiplicity conditions. As shown in Figure S6b, Supporting Information, the lithium symmetric cell of $Li//Li_3YBr_{5.7}F_{0.3}//Li$ was constructed at an initial current density of 0.05 mA cm^{-2}. The multiplication rate was increased in steps of 0.05 mA cm^{-2} before the current density increased to 0.5 mA cm^{-2}. The subsequent increase in multiplicity was in steps of 0.1 mA cm^{-2}. The lithium plating/stripping time of single step was 1 h. With a gradual increase in current density, the polarization voltage gradually grows. At a current density of 1.0 mA cm^{-2}, the polarization voltage drops off, indicating a micro-short circuit in the lithium symmetric cell. The CCD value of the $Li_3YBr_{5.7}F_{0.3}$ is ≈0.9 mA cm^{-2}. In order to verify the electrochemical cycling stability of the $Li_3YBr_{5.7}F_{0.3}$ for lithium metal at large lithium plating/stripping capacities, the behavior of cycling Li–Li symmetrical cell at 0.75 mA cm^{-2} with the capacity of 0.75 mAh cm^{-2} is displayed in Figure S6c, Supporting Information. This symmetric cell experiences a same activation process with the cell at 0.1 mA cm^{-2}. The overpotential increases from around 0.1 to 0.3 V in the initial 70 h. The cell exhibits a more intense interfacial response at 0.75 mA cm^{-2} compared to the lower current density. Until 300 h, the overpotential is gradually decreasing and keeping at a low level around 0.07 mV. This $Li//Li_3YBr_{5.7}F_{0.3}//Li$ symmetric cell can still display a stable cycling over 1000 h. In contrast, the CCD was at a lower level for $Li//Li_3YBr_6//Li$, reaching only 0.3 mA cm^{-2} before a short circuit occurs (Figure S6d, Supporting Information). At the same time, the lithium plating/stripping potential was at a high level, indicating the continuous side-reaction taking place at the interface and the accumulation of interfacial impedance. The poor cycling performance demonstrates that the instability of Li_3YBr_6 to the lithium metal.

To understand the process of formation of the interfacial layer between the electrolyte and lithium metal, time-resolved EIS was conducted. The semicircle region represents the impedance of the electrolyte at the interface with the lithium metal. The trend of the two electrolytes in first 50 h was almost the same as the time increases (Figure S7a,b, Supporting Information). At 15 h, the interface resistance of both electrolytes is at a high level. And then, the resistance dropped due to the improvement of contact. With the cycle continuing, the interfacial resistance of the symmetric cells with $Li_3YBr_{5.7}F_{0.3}$ returns to a lower level around 200 Ω (Figure S7b, Supporting Information). In contrast, the interfacial resistance of the symmetric cells with Li_3YBr_6 gradually increases to over 900 Ω (Figure S7a, Supporting Information). This result also confirms the trend of the curve in the symmetrical cells.

To research the protective mechanism of the reticular sheet at the interface, the chemical characterization of the interface after cycling was studied by XPS depth profiling. **Figure 3** presents the overall spectra evolution of Li 1s, Y 3d, and F 1s from the interface to Li metal with $Li_3YBr_{5.7}F_{0.3}$. The spectra evolution of Li 1s in different etch levels are exhibited as Figure 3a. The peaks at ≈56 eV mean binging energy of the Li in the $Li_3YBr_{5.7}F_{0.3}$. With the etch level increasing continually, the strongest signal intensities gradually shift to Li—F bonds at ≈55 eV and eventually shift to Li^0 at ≈54 eV. F 1s spectra exhibit the same evolution trend as Li 1s (Figure 3c). The characteristic peaks at ≈686.1 eV assigned to the F 1s in the $Li_3YBr_{5.7}F_{0.3}$. The characteristic peaks at ≈684.7 eV of Li—F bonds rise up gradually due to the formation of LiF compounds at the interface. The overall spectra evolution of Y 3d is shown as Figure 3e. The characteristic peaks of Y 3d in the $Li_3YBr_{5.7}F_{0.3}$ (Y3d3/2 at ≈160.6 eV and Y3d5/2 at ≈158.4eV) and Y—F bonds (Y3d3/2 at ≈161.6 eV and Y3d5/2 at ≈159.5 eV) both occur in the interface. With the etch level increasing, the characteristic peaks of Y—F bonds are gradually stronger, which indicated the formation of YF_x compounds at the interface.

The LiF and YF_x generated at the interfacial layer play a protective role on the solid electrolyte after cycling of the symmetric cell with $Li_3YBr_{5.7}F_{0.3}$. The F-rich robust layer inhibits the degradation of the SSE and significantly slows down the reduction process.

However, the Li_3YBr_6 overall spectra evolution trend of Li 1s, Y 3d, and F 1s at the interface is different compared with the $Li_3YBr_{5.7}F_{0.3}$ overall spectra. As shown in Figure S8a, Supporting Information, the characteristic peaks of Li—Br bonds appear in the interface (≈56.9 eV). The formation of LiBr compounds indicates that Li_3YBr_6 is degraded. The characteristic peaks of F 1s not occur (Figure S8c, Supporting Information). The overall spectra evolution of Y 3d is shown as Figure S8e, Supporting Information. In particular, only the characteristic peaks of Y 3d in the Li_3YBr_6 clearly occur. It is proved that no fluoride is formed at the interface. With the etch level increasing, signal intensities gradually reduce due to being close to the Li metal layer.

The morphology of Li metal after cycling 1000 h was studied by SEM. As shown in Figure S9, Supporting Information, the Li surface before cycling is very smooth (Figure S9a, Supporting Information). The Li surface of the cell with $Li_3YBr_{5.7}F_{0.3}$ is consecutive and homogeneous (Figure S9b, Supporting Information). Reticular sheets coating on the Li metal surface can be observed. These dense sheets at the interface protect SSE from reduction by Li metal and make the interface structure more stable, which allows the cell to maintain a stable cycle with less polarization. On the contrary, the Li surface of the cell with Li_3YBr_6 is cracked (Figure S9c, Supporting Information). The unlimited interfacial side reactions prevent the homogeneous deposition of lithium ions, which leads to excessive local stresses at the interface and eventually leads to the destruction of the interfacial structure. The lithium dendrite will grow along these cracks. The Li_3YBr_6 at the interface experience degradation with the cycling due to the successive interfacial

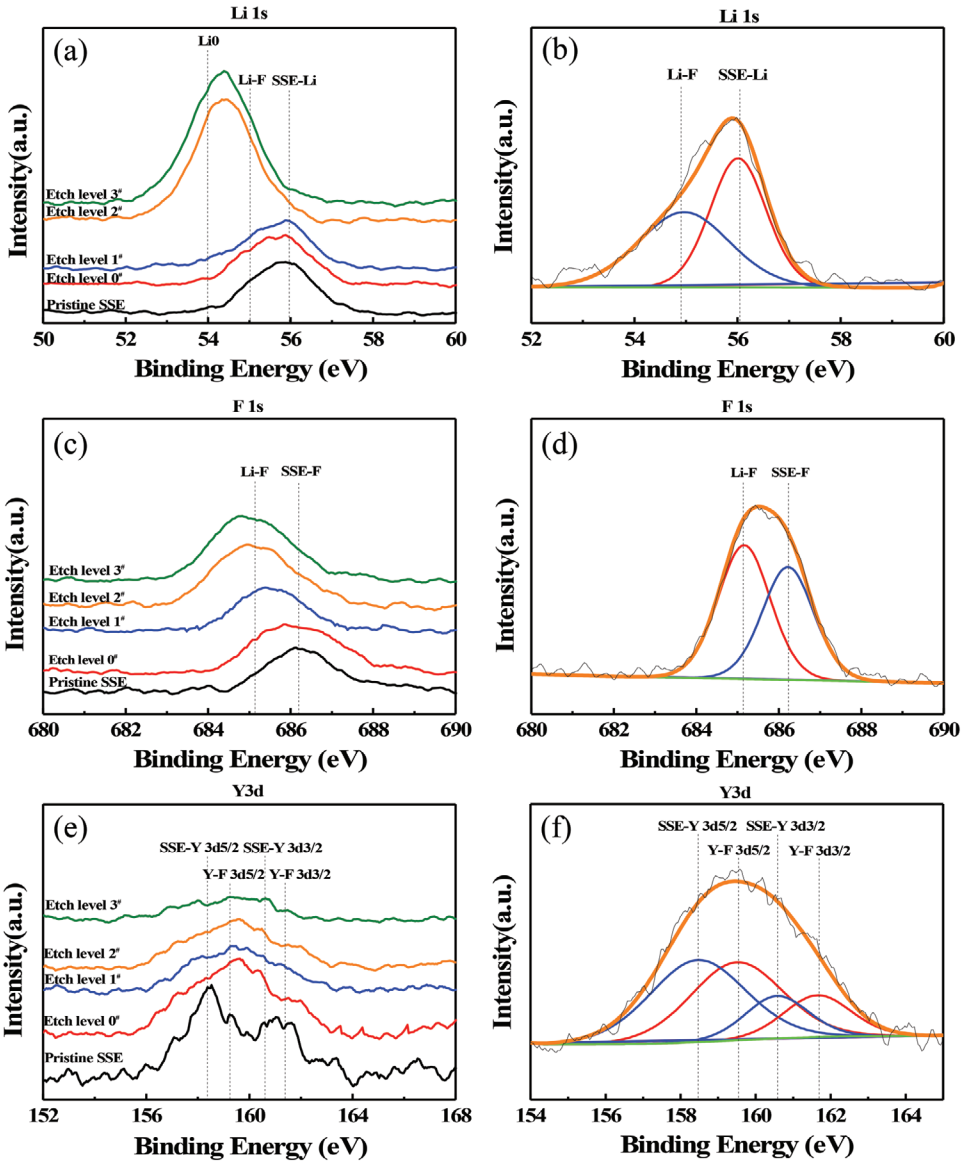

Figure 3. XPS depth profiling analysis. a,c,e) overall spectra evolution of Li 1s, F 1s, and Y 3d with different etch level at the Li/$Li_3YBr_{5.7}F_{0.3}$ interface. b,d,f) XPS spectra of Li 1s, F 1s, and Y 3d at the Li/$Li_3YBr_{5.7}F_{0.3}$ interface.

side reactions. The results of SEM agree well with the results of the curve of cycling Li–Li symmetrical cells.

In summary, dense and reticular structures were formed in situ at the interface between $Li_3YBr_{5.7}F_{0.3}$ and Li metal during cycling, which indicates that the $Li_3YBr_{5.7}F_{0.3}$ can protect lithium metal against reduction. At the same time, the existence of robust fluorinated interface can inhibit the reduction reaction and protect the interface structure between Li metal and SSE. The favorable stability of $Li_3YBr_{5.7}F_{0.3}$ against Li metal guarantees long cycling of the symmetric cell. In contrast, the Li_3YBr_6 without fluorine doping was unable to form a stable interface with the Li metal. The continuous side reactions lead to a large polarization at the interface. Degradation of the solid electrolyte occurs. The deterioration of the interface structure leads to interfacial contact failure. As a result, the interfacial resistance increases, which is not friendly to the stable cycle of the symmetric cell.

To demonstrate the advantages of in situ fluorinated passivation layers over artificial fluorinated passivation layers, artificial fluorinated modified Li symmetric cells with Li_3YBr_6 were assembled. The formation of an artificial fluorinated interfacial layer in the lithium symmetric cell is achieved by the introduction of an extra artificial source of fluorine in cycle. By adding a drop of high-concentration electrolytic solution with LiFSI on the Li metal pieces and drying under vacuum,[31] a fluoride-based interface layer will be formed in Li symmetric cells. As shown in Figure 2d, under current density of 0.1 mA cm^{-2}, the initial plating/stripping potential of the Li symmetric cell with artificial fluorinated layer is around 0.05 V. With the initial activation process, the plating/stripping potential increase to a maximum of 0.2 V due to the interface reaction. And then, the plating/stripping potential dropped to 0.01 V. The early cycling process was similar to the cell with $Li_3YBr_{5.7}F_{0.3}$ shown in Figure 2c, which

suggests that artificially fluorinated interfacial layers can achieve a passivation process similar to that of in situ interfacial layers. However, after cycling to 200 cycles, the plating/stripping potential occurs as an uninhibited increase of more than 2.0 V. The artificially fluorinated interface cannot achieve a homogeneous distribution of fluoride. The solid contact at the interface is poor. A high number of gaps exist at the interface, where lithium dendrites appear to grow. As the cycle proceeds further, the lithium dendrites gradually pass through the fluorinated layer and come into direct contact with the solid electrolyte directly, thus activating a new uninhabitable reduction. The in situ fluorinated interfacial layer is more conducive to long-cycle interfacial protection. At the same time, the adoption of fluorinated electrolytes reduces the processes involved in cells assembly, which is an important advantage in practical applications.

In order to understand the polarization of the artificial fluoride interface during different cycles, the symmetric cells with 200 and 500 h cycles were disassembled for XPS testing (Figure S10, Supporting Information). Compared to the pristine Li_3YBr_6, a significant fluoride response appears at the interface after 200 h of cycling. The characteristic peaks of Li—F bonds at ≈55 and at ≈684.7 eV in the spectra evolution of Li 1s and F 1s are occurred (Figure S10a,b, Supporting Information), which indicated that a fluoride-rich passivation layer is generated at the interface to inhibit the reduction process. The results are consistent with the symmetric cells of the in situ fluoride interface at the same cycles. However, the inhibition effect of artificial fluorinated interfacial layers is still limited compared to in situ fluorinated interfacial layers. When 500 h of cycling, the characteristic peaks of Li—Br bonds appear in the interface although fluoride is still present. The characteristic peaks of Li—Br bonds at ≈56.9 eV indicates that Li_3YBr_6 is degraded (Figure S10d, Supporting Information). The decomposition of the Li_3YBr_6 proves the failure of the artificial fluoride passivation layer to achieve inhibition of the reduction reaction under long cycling conditions.

In order to have a further understanding of the in situ interface between $Li_3YBr_{5.7}F_{0.3}$ and lithium metal, DFT calculations were performed on the constructed fluorinated interface model. Different linear combinations of electrolyte components were performed. The different combinations of the equilibrium-stable phases are evaluated quantitatively by calculating the normalized energy of each atom (E-hull). The composition of the electrolyte after F-doping can be interpreted as Equation (3):

$$Li_3YBr_{6-x}F_x = x/6\,(Li_3YF_6) + (1-x/6)\,(Li_3YBr_6) \quad (3)$$

As shown in Table S2, Supporting Information, the stability of the Li_3YF_6 component is significantly lower than that of the Li_3YBr_6 component. When $x \leq 0.3$, the F-doped electrolyte remains in the equilibrium stable phase. However, at the beginning of the electrochemical cycle, there is a large polarization at the interface, which causes the unstable fluoride component to be prone to decomposition, thus gradually forming a fluorinated interfacial layer.

To prove the application potential of $Li_3YBr_{5.7}F_{0.3}$ with Li metal, the ASSLBs were constructed by using Li metal, LIC coated LCO (LCO@LIC) mixed $Li_3YBr_{5.7}F_{0.3}$ as the cathode, and $Li_3YBr_{5.7}F_{0.3}$ as the SSE layer. The mass of the LCO is ≈10 mg cm^{-2}. The voltage window of ≈2.5–4.2 V (versus Li/Li$^+$) was employed in charge and discharge at 0.14 mA cm^{-2}. The first curve are displayed as **Figure 4**a. Before the charging plateau of 3.78 V, there is only a small slope due to the effect of inevitable space charge. No extra voltage

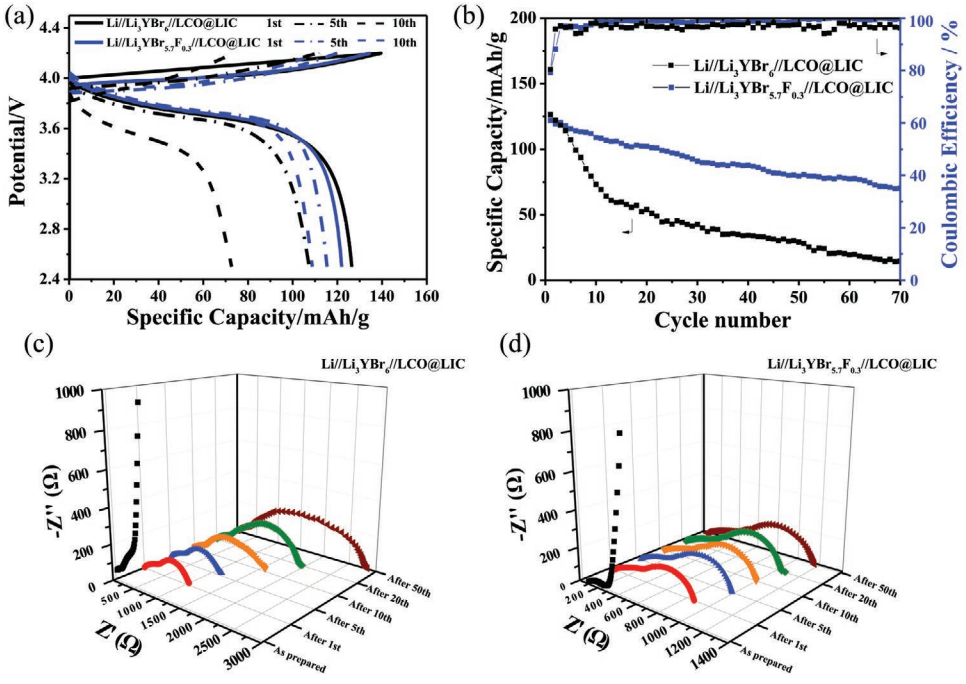

Figure 4. a) First, fifth, and tenth charge-discharge curves of the Li//Li_3YBr_6//LCO@LIC and Li//$Li_3YBr_{5.7}F_{0.3}$//LCO@LIC cells. b) Cycling stability of the Li//$Li_3YBr_{5.7}F_{0.3}$//LCO@LIC cell and the Li//Li_3YBr_6//LCO@LIC cell. Electrochemical impedance spectroscopy of c) Li//Li_3YBr_6//LCO@LIC and d) Li//$Li_3YBr_{5.7}F_{0.3}$//LCO@LIC cell recorded at different cycles.

plateau/slope can be found, which indicate that there is no side reaction on cathode or anode. In the Li//Li_3YBr_6//LCO@LIC cell, the first discharge specific capacity is up to 126.7 mAh g^{-1}. The first coulombic efficiency reaches 89%. In the Li//$Li_3YBr_{5.7}F_{0.3}$//LCO@LIC cell, the first discharge specific capacity is 121.6 mAh g^{-1} and the first coulombic efficiency reaches 90%, which reaches the close level of the Li//Li_3YBr_6//LCO@LIC cell. The discharge capacity of the Li//$Li_3YBr_{5.7}F_{0.3}$//LCO@LIC cell is stable in 70 cycles with the capacity retention stands at 60% (Figure 4b). The coulombic efficiency remains around 99%. By contrast, the discharge capacity of the Li//Li_3YBr_6//LCO@LIC cell is false in 70 cycles with the capacity retention standing at 12%. Without the protection of the robust layer, the interface reaction is continuous. The resultant degradation of Li_3YBr_6 eventually causes the destruction of the interface structure and the loss of solid–solid contact, which affects the cycle performance of the cell. The full cell with $Li_3YBr_{5.7}F_{0.3}$ suffers from instability problems as well as a large capacity degradation. The continuous and irreversible lithium loss should occur during the cycling of the full cell, resulting in a continuous capacity degradation. The exact reason of the instability of the full cell is subject to further experimental investigation.

The EIS evolution at different cycles is shown in Figure 4c,d. Two obvious semicircles can be observed in each plot. It is reported that LIC is stable with LCO,[19] so the high-frequency semicircle is mainly contributed by the interfacial resistance between composite cathode and SSEs. The middle-frequency semicircle is contributed by the interfacial resistance between Li metal and SSEs. The interfacial resistance of cathode and SSEs in each plot remains the level at 314 Ω. But the interfacial resistances of anode and SSEs in each cell with different SSEs display different results. The interfacial resistance of anode and Li_3YBr_6 increases obviously (Figure 4c). At the 50th cycle, the resistance reaches around 3000 Ω, which is the reason why the capacity of the cell of Li//Li_3YBr_6//LCO@LIC decreased quickly. However, the interfacial resistance of anode and $Li_3YBr_{5.7}F_{0.3}$ shows slow growth (Figure 4d); only a 300 Ω increase from the first to the 50th cycle. The almost unchanged interfacial resistance reflected that a stabilized interface gradually formed during cycling. So the capacity of the cell of Li//$Li_3YBr_{5.7}F_{0.3}$//LCO@LIC decreased more slowly.

The above results demonstrate that a fluoride-rich interfacial layer is formed in situ between the lithium metal and the electrolyte during the cycling process of a cell loaded with a fluorine-containing electrolyte. The fluoride-rich interfacial passivation layer effectively hinders the interfacial reaction process. Due to the protection of the passivation layer, a high solid–solid contact area is achieved at the interface. The improved solid–solid contact facilitates the transport of lithium ions. The cycling performance of the cell is enhanced in this way.

3. Conclusions

In conclusion, a new metal-halide electrolyte, fluorinated $Li_3YBr_{5.7}F_{0.3}$, not only with high ionic conductivity (1.8×10^{-3} S cm^{-1}) but also can directly work with Li metal anode have been proposed. The fluorinated $Li_3YBr_{5.7}F_{0.3}$ has a similar structure to Li_3YBr_6, while it shows much better stability when contact to Li anode. The Li plating/stripping can maintain over 1000 h at 0.75 mA cm^{-2} by only using $Li_3YBr_{5.7}F_{0.3}$ as electrolyte. Detail analysis suggests that the high stability of $Li_3YBr_{5.7}F_{0.3}$ electrolyte with Li metal is originated from the in situ formed fluoride-containing interface layer, which is dense and reticular. The homogeneous morphology in the in situ formed fluoride-containing interface layer inhibits the growth of Li dendrites and stabilizes the interface attaching, so as to guarantee long term protection. Compared to artificial fluorinated layers on the surface of Li, the formation of in situ fluorinated layers in the cycling process exhibit higher contact areas and uniform distribution, which contributes to high cycle stability. Furthermore, an improved performance is obtained in Li//$Li_3YBr_{5.7}F_{0.3}$//LCO@LIC full battery, which can charge and discharge stably over 70 cycles with the capacity retention higher than 60%. The fluorinating halide SSEs is expected to make an important exploration towards the development of electrolyte materials and high performance ASSLBs.

Supporting Information

Supporting Information is available from the Wiley Online Library or from the author.

Acknowledgements

This work was also supported by the Innovation Fund Project of GRINM (No. 2020TS0301). This work was also supported by Natural Sciences and Engineering Research Council of Canada (NSERC), Canada Research Chair Program (CRC), and Western University. This work was supported by the Guangdong Provincial Science and Technology Commission, Guangdong Key Areas R&D Program (2020B0909030004) and the Beijing Natural Science Foundation Committee, Haidian Original Innovation Joint Fund Project (L182023).

Conflict of Interest

The authors declare no conflict of interest.

Data Availability Statement

Research data are not shared.

Keywords

all-solid-state lithium batteries, halides, in situ interfaces, lithium metal anodes

Received: June 22, 2021
Revised: July 19, 2021
Published online:

[1] a) J. B. Goodenough, Y. Kim, *Chem. Mater.* **2010**, *22*, 587; b) K. Takada, *Acta Mater.* **2013**, *61*, 759; c) L. O. Hagman, P. Kierkegaard, P. Karvonen, A. I. Virtanen, J. Paasivirta, *Acta*

Chem. Scand. **1968**, *22*, 1822; d) Y. Kato, K. Kawamoto, R. Kanno, M. Hirayama, *Electrochemistry* **2012**, *80*, 749.
[2] a) S. S. Zhang, M. H. Ervin, K. Xu, T. R. Jow, *Electrochim. Acta* **2004**, *49*, 3339; b) M. Baba, N. Kumagai, N. Fujita, K. Ohta, K. Nishidate, S. Komaba, H. Groult, D. Devilliers, B. Kaplan, *J. Power Sources* **2001**, *97*, 798.
[3] X. C. Dong, L. Wang, *Prog. Chem.* **2005**, *17*, 248.
[4] N. Ohta, K. Takada, L. Zhang, R. Ma, M. Osada, T. Sasaki, *Adv. Mater.* **2006**, *18*, 2226.
[5] C. H. Chen, S. Xie, E. Sperling, A. S. Yang, G. Henriksen, K. Amine, *Solid State Ionics* **2004**, *167*, 263.
[6] X. X. Xu, Z. Y. Wen, X. L. Yang, L. D. Chen, *Mater. Res. Bull.* **2008**, *43*, 2334.
[7] F. Du, N. Zhao, Y. Li, C. Chen, Z. Liu, X. Guo, *J. Power Sources* **2015**, *300*, 24.
[8] Z. Xiao, S. Chen, M. Guo, *Trans. Nonferrous Met. Soc. China* **2011**, *21*, 2454.
[9] X. Han, Y. Gong, K. Fu, X. He, G. T. Hitz, J. Dai, A. Pearse, B. Liu, H. Wang, G. Rubloff, *Nat. Mater.* **2016**, *16*, 572.
[10] R. Kanno, M. Maruyama, *J. Electrochem. Soc.* **2001**, *148*, A742.
[11] K. Kaup, J. D. Bazak, S. H. Vajargah, X. Wu, J. Kulisch, G. R. Goward, L. F. Nazar, *Adv. Energy Mater.* **2020**, *10*, 1902783.
[12] Y. Seino, T. Ota, K. Takada, A. Hayashi, M. Tatsumisago, *Energy Environ. Sci.* **2014**, *7*, 627.
[13] R. Rao, S. Adams, *Phys. Status Solidi* **2011**, *208*, 1804.
[14] N. Kamaya, K. Homma, Y. Yamakawa, M. Hirayama, R. Kanno, M. Yonemura, T. Kamiyama, Y. Kato, S. Hama, K. Kawamoto, *Nat. Mater.* **2011**, *10*, 682.
[15] Y. Kato, S. Hori, T. Saito, K. Suzuki, M. Hirayama, A. Mitsui, M. Yonemura, H. Iba, R. Kanno, *Nat. Energy* **2016**, *1*, 16030.
[16] T. Famprikis, P. Canepa, J. A. Dawson, M. S. Islam, C. Masquelier, *Nat. Mater.* **2019**, *42*, 163.
[17] N. Ohta, K. Takada, I. Sakaguchi, L. Zhang, R. Ma, K. Fukuda, M. Osada, T. Sasaki, *Electrochem. Commun.* **2007**, *9*, 1486.
[18] Y. J. Nam, D. Y. Oh, S. H. Jung, Y. S. Jung, *J. Power Sources* **2018**, *375*, 93.
[19] X. Li, J. Liang, J. Luo, M. N. Banis, C. Wang, W. Li, S. Deng, C. Yu, F. Zhao, Y. Hu, T.-K. Sham, L. Zhang, S. Zhao, S. Lu, H. Huang, R. Li, K. R. Adair, X. Sun, *Angew. Chem., Int. Ed.* **2019**, *58*, 16427.
[20] T. Asano, A. Sakai, S. Ouchi, M. Sakaida, A. Miyazaki, S. Hasegawa, *Adv. Mater.* **2018**, *30*, 1803075.
[21] R. Schlem, S. Muy, N. Prinz, A. Banik, Y. H. Shao, M. Zobel, W. G. Zeier, *Adv. Energy Mater.* **2020**, *10*, 1903719.
[22] J. Liang, X. Li, S. Wang, K. R. Adair, W. Li, Y. Zhao, C. Wang, Y. Hu, L. Zhang, S. Zhao, S. Lu, H. Huang, R. Li, Y. Mo, X. Sun, *J. Am. Chem. Soc.* **2020**, *142*, 7012.
[23] L. Zhou, C. Y. Kwok, A. Shyamsunder, Q. Zhang, X. Wu, L. F. Nazar, *Energy Environ. Sci.* **2020**, *13*, 2056.
[24] K. H. Park, K. Kaup, A. Assoud, Q. Zhang, X. Wu, L. F. Nazar, *ACS Energy Lett.* **2020**, *5*, 533.
[25] S. Wang, Q. Bai, A. M. Nolan, Y. Liu, S. Gong, Q. Sun, Y. Mo, *Angew. Chem.* **2019**, *131*, 8123.
[26] K. Fajan, *Naturwissenschaften* **1923**, *11*, 165.
[27] X. Li, J. Liang, X. Yang, K. R. Adair, C. Wang, F. Zhao, X. Sun, *Energy Environ. Sci.* **2020**, *13*, 1429.
[28] Y. Han, S. H. Jung, H. Kwak, S. Jun, H. H. Kwak, J. H. Lee, S.-T. Hong, Y. S. Jung, *Adv. Energy Mater.* **2021**, *11*, 2100126.
[29] L. M. Riegger, R. Schlem, J. Sann, W. G. Zeier, J. Janek, *Angew. Chem., Int. Ed.* **2020**, *60*, 6718.
[30] S. Wenzel, T. Leichtweiss, D. Krüger, J. Sann, J. Janek, *Solid State Ionics* **2015**, *278*, 98.
[31] X. Fan, X. Ji, F. Han, J. Yue, J. Chen, L. Chen, T. Deng, J. Jiang, C. Wang, *Sci. Adv.* **2018**, *4*, eaau9245.